Bifurcation enhances temporal information encoding in the olfactory periphery

Kiri Choi[a,b,c,1], Will Rosenbluth[a,1], Isabella R. Graf[b,d], Nirag Kadakia[a,b,c,2], and Thierry Emonet[a,b,d,e,2]

[a]Department of Molecular, Cellular, and Developmental Biology, Yale University, New Haven, CT, 06511; [b]Quantitative Biology Institute, Yale University, New Haven, CT, 06511; [c]Swartz Foundation for Theoretical Neuroscience, Yale University, New Haven, CT, 06511; [d]Department of Physics, Yale University, New Haven, CT, 06511; [e]Interdepartmental Neuroscience Program, Yale University, New Haven, CT, 06511

[1]K.C. and W.R. contributed equally to this work.

[2]To whom correspondence may be addressed.

Email: nirag.kadakia@yale.edu or thierry.emonet@yale.edu.

Abstract

Living systems continually respond to signals from the surrounding environment. Survival requires that their responses adapt quickly and robustly to the changes in the environment. One particularly challenging example is olfactory navigation in turbulent plumes, where animals experience highly intermittent odor signals while odor concentration varies over many length- and timescales. Here, we show theoretically that *Drosophila* olfactory receptor neurons (ORNs) can exploit proximity to a bifurcation point of their firing dynamics to reliably extract information about the timing and intensity of fluctuations in the odor signal, which have been shown to be critical for odor-guided navigation. Close to the bifurcation, the system is intrinsically invariant to signal variance, and information about the timing, duration, and intensity of odor fluctuations is transferred efficiently. Importantly, we find that proximity to the bifurcation is maintained by mean adaptation alone and therefore does not require any additional feedback mechanism or fine-tuning. Using a biophysical model with calcium-based feedback, we demonstrate that this mechanism can explain the measured adaptation characteristics of *Drosophila* ORNs.

Introduction

Successful olfactory navigation depends on the ability of animals to make informed navigational decisions, which in turn requires accurate sensory processing to extract relevant information from odor signals. Animals navigate turbulent odor plumes (1-3) by turning upwind when they detect odor and crosswind otherwise (4-13). For this strategy to be successful, they must extract from the signal not only the intensity of the odor filaments they encounter but also temporal information, such as when and how frequently odor filaments arrive, how long they last, and when they end (Fig. 1A) (4, 8, 14-20). Information about the timing of odor signals is also critical for detecting the direction of motion of odor filaments (21) and resolving odor sources in space (15, 17). To reliably extract such information from an odor signal, the olfactory system must adapt its sensitivity to the ambient statistics of the odor concentration, which in turbulent plumes can span orders of magnitude (1-3, 22).

Odor detection starts with odorant molecules binding to olfactory receptors (ORs). Different types of ORs are expressed in the corresponding olfactory receptor neurons (ORNs), which share similar response functions but with shifted sensitivities (23, 24). In *Drosophila*, ORNs adapt their gain in response to changes in mean odor intensity according to Weber-Fechner's law (25, 26). Adaptation to the mean signal intensity takes place upstream of the firing machinery at the level of the receptors via a feedback mechanism involving calcium (25-29). ORNs also display finite yet rapid adaptation

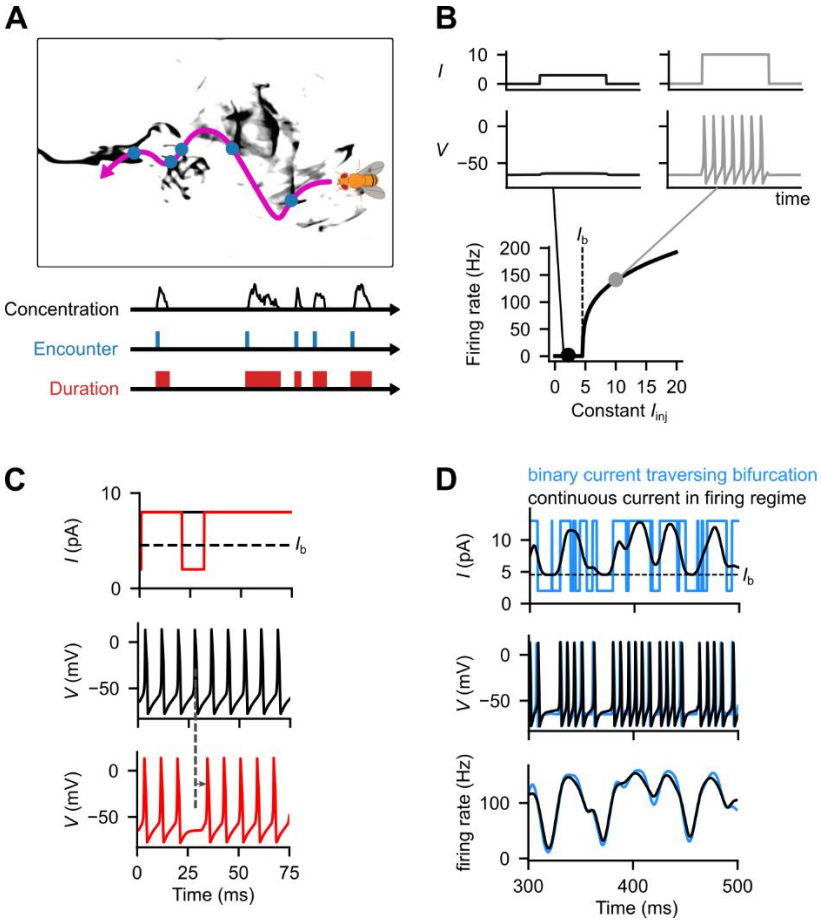

Fig. 1. Firing rates for continuous current waveforms can be approximated by binary switching currents crossing the spiking threshold. (A) Flies navigate odor plumes using information about the intensity and timing of the odor fluctuations they encounter. **(B)** The response dynamics of a neuron spiking above and below the firing threshold. Top: Input current over time for a current temporarily above (right, grey) and below (left, black) the firing threshold. Middle: corresponding membrane voltage over time. Bottom: Average firing rate r as a function of a fixed input current. The simulated neuron is quiescent below the threshold current I_b, while the firing rate suddenly and monotonically rises with the current above the threshold. **(C)** For dynamic (non-static) currents, the dose-response curve from (B) may not apply. Top: a static current (black) and a current with a brief dip below the firing threshold (red). Middle and bottom plots: corresponding neuron membrane voltages for two currents. For the current with a dip, the neuron crosses into a non-firing regime and causes a brief delay in spikes, compared to the response to the static current (dotted line and arrow). This delay will manifest as a reduction – but not zeroing – of the firing rate, obscuring the fact that the neuron is crossing into a quiescent state. **(D)** Extrapolating from (C), the response of the neuron to a fluctuating but continuous current that always remains within the firing regime, i.e., above I_b (top, black), produces membrane voltages (middle, black) and firing rates (bottom, black) that can be well-approximated by a binary current that continuously crosses I_b, provided the switch points are chosen judiciously (blue).

to changes in the signal variance via an unknown mechanism that involves both signal transduction and the firing machinery (29). Finally, measurements of the cross-correlations between odor signal and firing rate show that *Drosophila* ORNs maintain a high degree of temporal precision, where the delay between odor onset and firing response stays invariant to mean odor intensity (24, 27, 29, 30). Together, these adaptation properties suggest that ORNs can precisely and robustly encode

the timing and intensity of fluctuations in the odor signal, but the mechanism underlying such precision remains unclear.

When *Drosophila* ORNs are exposed to a fluctuating odor signal of constant but low mean intensity, the firing rate exhibits a bimodal distribution (29), indicating that the neuron is transitioning between a state of "firing" and "resting." This observation strongly suggests that the neuron is operating near a bifurcation of the firing machinery, consistent with past computational studies on contrast adaptation (31-34).

To further examine the implications of this observation, consider a spiking conductance-based neuron model built on the Hodgkin-Huxley framework, which relates changes in intracellular ion concentrations to changes in the membrane voltage. As the injected current crosses a firing threshold, the model exhibits a qualitative change in dynamics from a constant voltage to periodic spiking (Fig. 1B). In the theory of nonlinear dynamical systems, such transitions are known as bifurcations; accordingly, we define the firing threshold as the bifurcation point and the corresponding current as I_{b}. For constant currents above I_{b}, the voltage spikes periodically and the firing rate stays constant, while the neuron does not fire below the firing threshold. In the firing regime, neurons increase their firing rate monotonically with injected current (Fig. 1B). But near I_{b}, the distinction between the "firing" and "resting" states is more ambiguous. Consider a brief change in current, from above I_{b} to below I_{b} and back above (Fig. 1C). While the neuron has technically switched between two states, this state change is masked in the voltage trace, which only exhibits a delay in spike timing and therefore a brief reduction in firing rate. Thus, for *dynamic* input currents near I_{b}, the neuron can act much like it does above I_{b} – encoding signals with a continuous-value firing rate rather than as a discrete 2-state ON/OFF system (Fig. 1D).

In this paper, we investigate how proximity to a bifurcation of the firing dynamics in ORNs contributes to odor information encoding. We use a Morris-Lecar type model (35), a highly simplified membrane dynamics model in the Hodgkin-Huxley family, whose phase space is fully described in two dimensions. We show that proximity to the bifurcation enables variance adaptation and enhances the encoding of information about the timing, duration, and intensity of odor fluctuations, such as those experienced by an animal in turbulent plumes. We devise a biophysical model of *Drosophila* ORNs incorporating calcium dynamics, which achieves intrinsic adaptation to the signal mean and thereby also provides variance adaptation by keeping the neuron near the bifurcation.

Results

Intrinsic variance adaptation irrespective of bifurcation type. *Drosophila* ORNs intrinsically adapt their response to changes in signal variance (29), allowing them to adjust their sensitivity to the given odor signal. Previous studies have proposed that neurons constantly crossing the firing threshold can implement a simple strategy for intrinsic variance adaptation (32, 34, 36). Here, we demonstrate intrinsic variance adaption due to proximity to a bifurcation and characterize the adaptive behavior against different bifurcation types. We use a 2-dimensional Hodgkin-Huxley conductance-based neuron model known as the Morris-Lecar model (Na+K model) (35), in which inward-flowing Na+ and outward-flowing K+ channels drive spike generation. We drive the neuron model with a fluctuating current $I(t)$ defined by an Ornstein-Uhlenbeck (O-U) stochastic process with input correlation timescale τ_s, standard deviation σ, and mean μ. Once the spikes are generated, we compute the firing rate $r(t)$ by convolving the binary sequence of threshold voltage crossings with a linear filter with timescale τ_r (Fig. 2A, see Methods).

When we drive the Na+K model with a fluctuating O-U input current $I(t)$ but with the mean around the bifurcation point (e.g., $\mu = I_{\mathrm{b}} = 4.54\ pA$), we see a smooth, continuous response much like in a traditional I-r curve (Fig. 2B), unlike the dose-response derived for constant, non-fluctuating

signals (Fig. 1B). However, the I-r curve has a distinct dependence on the amount of signal fluctuation σ. Inputs with higher variance (Fig. 2B, dark red) have broader I- r curves. When the input drops below I_b, changes in the firing rate only depend on the excursion time below I_b but not on the magnitude of the drop. Since this excursion time depends on the input correlation timescale of the O-U input, rescaling the input by its σ collapses the distinct I-r curves onto a single curve when $I < I_\mathrm{b}$ (Fig. 2C), indicating intrinsic adaption to the variance of the input.

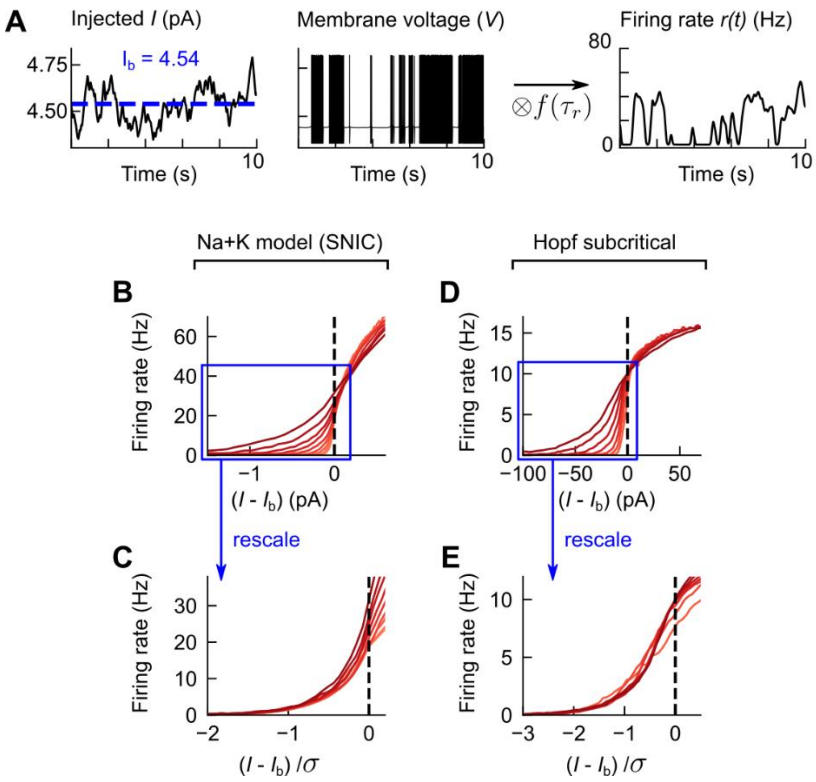

Fig. 2. The dose-response of conductance-based neuron models is intrinsically adaptive (invariant) to input signal variance regardless of the bifurcation type. (A) A schematic showing how input current is translated to firing rate in a conductance-based neuron model. Here, the input current $I(t)$ is modeled as an O-U process with input correlation timescale $\tau_s = 200\ ms$, mean $\mu = 4.54\ pA$, and standard deviation $\sigma = 0.1$. The firing rates are calculated by binarizing and filtering the spikes with an exponential filter f with firing rate filter timescale τ_r. This model has Na+ and K+ channels driving action potentials and fires when the injected current is above $I_\mathrm{b} = 4.54\ pA$. **(B)** Dose-response curves of the firing rate as a function of the input current difference from the firing threshold ($I_\mathrm{b} = 4.54\ pA$) obtained from the Na+K model with an SNIC bifurcation. The different curves correspond to increasing fluctuations with size σ, ranging from $\sigma = 0.04\ pA$ (light red) to $1.6\ pA$ (dark red). **(C)** When rescaled by the magnitude of σ, the dose-response curves collapse to a single curve, implying that the system inversely adapts its gain with σ. **(D)** Dose-response curves from a neuron model with a Hopf subcritical bifurcation, where the firing rate is discontinuous at the threshold current $I_\mathrm{b} = 101\ pA$. **(E)** The same plot with the *x*-axis rescaled by σ, as in (C).

The bifurcation-induced variance adaptation is not unique to this model. Though neurons can differ widely in their response properties, the nature of the quiescence-to-firing bifurcation falls into only a few universality classes. The Na+K model exhibits a saddle node on an invariant circle (SNIC) bifurcation, in which the spiking frequency goes arbitrarily close to zero near I_b. Another common bifurcation observed in neurons is a Hopf bifurcation, which exhibits a discontinuity in the

frequency-current response and can be either subcritical or supercritical. When modeling a spiking neuron model exhibiting a Hopf bifurcation (see Methods), we observed a similar collapse of the I-r curves despite the different spiking behavior near the critical current I_b exhibited by the two models (Fig. 2D, E). Note that precise adaptation breaks down above the bifurcation point due to the nonlinear yet monotonic relationship between the input and the firing rate in this regime. In a simpler threshold model, where the magnitude of the signal is fully binarized, adaptation occurs both above and below the threshold (34), unlike in the neuron models considered here.

Bifurcation helps maintain coding capacity across signal variance. When navigating an odor environment, flies need to detect and integrate various features from the odor signal. We quantify the coding capacity of a neuron by calculating the mutual information (MI) between input current I and firing rate r, defined as

$$MI(I,r) = \sum_I P(I) \sum_r P(r|I) \log P(r|I) - \sum_r P(r) \log P(r)\,, \qquad [1]$$

where $P(I)$ and $P(r)$ are the probability distributions of the current and firing rate, respectively (see Methods). Like above, we use as input a correlated O-U current with a mean equal to the bifurcation current I_b and verified that the numerical MI calculation is robust to the binning process (see *SI Appendix*, Fig. S1). Since scaling of the I-r curve with signal strength σ only occurs when the current is below the bifurcation point (Fig. 2C, E), we consider two separate quantities, MI and MI-, defined as the mutual information calculated over the entire signal and the mutual information calculated over only the times when the signal is below the threshold ($I < I_\mathrm{b}$), respectively. MI- quantifies the contribution of the sub-threshold regime to the information transfer. MI- and MI encode different types of information used by animals during odor-guided navigation. Intuitively, mutual information below the bifurcation point (MI-) is correlated to the time since the last odor encounter. In contrast, mutual information over the entire signal (MI) encodes the relative changes in the odor concentration.

We find that MI monotonically increases as σ increases over two orders of magnitude (Fig. 3A). This is expected since a highly variable odor landscape leads to a wider range of signal and response magnitudes. In contrast, MI- is largely independent of σ (Fig. 3B, Fig. S2) since for inputs below I_b, adaptation to variance in the input automatically takes place. Furthermore, the MI- distribution is asymmetric with respect to I_b, as the amount of encoded information quickly diminishes when $\mu < I_\mathrm{b}$. Generally, when σ is small and μ is far from the bifurcation point, the rate of threshold crossing goes down, leading to a decrease in MI. For MI-, this effect is exacerbated when $\mu < I_\mathrm{b}$ since spiking occurs too sporadically to maintain the firing rate, eventually yielding zero firing rate for most times when $I < I_\mathrm{b}$. Finally, MI- stays elevated over a range of filter time scales τ_r (Fig. 3C, D).

MI characteristics are closely related to the mechanistic origin of the variance adaptation near I_b. When the model neuron generates spike events from an input, this amounts to a binarization of the signal (Fig. 2A). If we considered the mutual information between a static, temporally uncorrelated signal and its response (as in Fig. 1B), MI would not exceed 1 bit and MI- would be 0. However, in the neuron model, the observed MI is significantly higher than 1 bit due to the temporal correlation present in the input signal and thereby in the firing rates (34, 37). Since this correlation persists over the input correlation timescale τ_s, the coding capacity of the neuron depends on the relative magnitude of the input timescale τ_s and the filtering rate timescale τ_r. When $\tau_r \gg \tau_s$, all fluctuations average out, and MI barely exceeds 0 bit (Fig. 3D). When $\tau_r \ll \tau_s$, the output converges to a binary time series, and MI does not exceed 1 bit (and 0 bit for MI-). Calculating MI- for a range of input and filtering timescales, we find that the optimal coding capacity lies on the manifold $\tau_r \sim \tau_s/10$ (Fig. 3D; Fig. S3), consistent with observations in a simpler binary switching model (34).

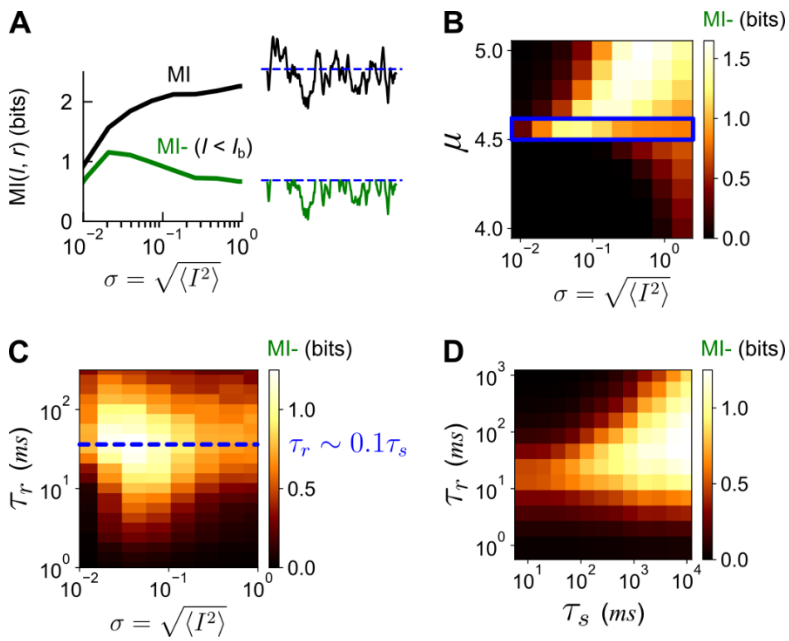

Fig. 3. Bifurcation-induced variance adaptation maintains coding capacity. (A) Mutual information between the distribution of input current I (modeled as an O-U process with mean μ, standard deviation σ, and correlation timescale $\tau_s = 500\,ms$) and the firing rate r as a function of the strength of the fluctuations in the input current (MI, black). Green: same but only for currents below the threshold ($I < I_b$, MI-). MI increases monotonically with the signal variance. Meanwhile, MI- remains largely independent of the signal variance over two orders of magnitude. The firing rate filter timescale is $\tau_r = 55\,ms$. **(B)** MI- as a function of the mean μ and standard deviation σ of the input current. The blue box corresponds to $\mu \sim I_b = 4.54\,pA$. **(C)** MI- as a function of σ and τ_r. MI- is maximized when $\tau_r = 40\,ms$, which is $\sim 1/10$ of the input τ_s (blue dashed line). **(D)** MI- as a function of τ_s and τ_r shows that information transfer is bounded by the constraint $\tau_r \lesssim 1/5\,\tau_s$ and large enough input timescale τ_s to cover the inter-spike interval.

This insight can be exploited to improve coding capacity in traditional linear-nonlinear (LN) neuron models (see *SI Appendix*) consisting of a Gaussian filter followed by a rectified linear unit (ReLU). Standard LN models do not exhibit variance adaptation (Fig. S4, red). However, substituting the ReLU for the SNIC bifurcating I-r curve (Fig. 1B), we see an imperfect gain control (Fig. S4, orange) since the response changes are magnified for transitions between the active and quiescent states but diminished within the active state. Additionally, switching the order of operation from LN to nonlinear-linear (NL) shows a significant improvement (~15%) in coding capacity (Fig. S4C) while keeping the gain adaptation (Fig. S4, blue). Compared to standard LN models, this new architecture better reflects the generation of firing rates from spiking neurons and significantly improves the approximation of sensory neuron dynamics.

Bifurcation enhances information encoding from temporal odor cues. In turbulent odor environments, animals use the timing of their encounters with odor filaments to decide when to orient upwind or crosswind (2, 8, 20, 38, 39). Here, we examine how the ORN's ability to encode odor timing information varies with the proximity to the bifurcation. We used the critical current value I_b as the threshold to define when the signal is detected or not. As temporal cues of interest, we consider Δt_{ON}, the time difference between subsequent positive crossings of the threshold; Δt_{OFF}, the time difference between subsequent negative crossings of the firing threshold; t_{dur}^{enc}, the duration of 'odor encounters' (signal above the firing threshold); and t_{dur}^{bnk}, the duration of 'blanks' (signal below the firing threshold) (Fig. 4A). From our simulations, we obtain the stationary distributions of

Δt_{ON}, Δt_{OFF}, $t_{\mathrm{dur}}^{\mathrm{enc}}$, and $t_{\mathrm{dur}}^{\mathrm{bnk}}$ and calculate the mutual information between these distributions and that of the firing rate r.

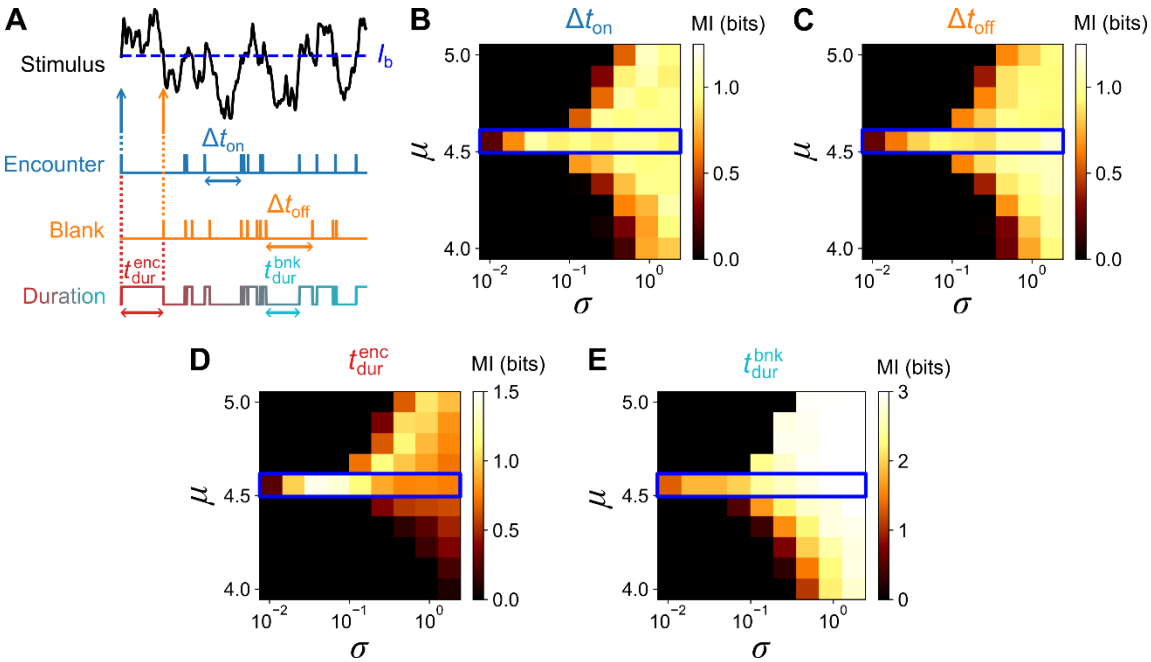

Fig. 4. The coding capacity of signal timing is elevated when ORN is proximal to the bifurcation point. (A) A schematic illustrating different temporal statistics that ORNs may encode for odor-guided navigation. Odor encounters and odor blanks correspond to the stimulus crossing the firing threshold from below/above. The timings between subsequent encounters or blanks are defined as Δt_{ON} and Δt_{OFF}, respectively. The duration of odor encounters $t_{\mathrm{dur}}^{\mathrm{enc}}$ and blanks $t_{\mathrm{dur}}^{\mathrm{bnk}}$ denote the time from an encounter to a blank or a blank to an encounter, respectively. **(B)** MI between the distribution of encounter times Δt_{ON} and the firing rate r as a function of signal mean μ and standard deviation σ. MI increases and saturates as encounter frequency increases, which depends on the relative values of μ and σ. When μ is close to $I_{\mathrm{b}} = 4.54\ pA$ (blue box), information about Δt_{ON} is encoded over the widest range of σ. **(C-E)** Same as (B) for the distributions of blank times Δt_{OFF}, encounter duration $t_{\mathrm{dur}}^{\mathrm{enc}}$, and blank duration $t_{\mathrm{dur}}^{\mathrm{bnk}}$. Unlike other temporal cues, information about encounter duration becomes small when $\mu < I_{\mathrm{b}}$.

We find that significant information about the signal timing is encoded across a range of mean μ and standard deviation σ of the input current (Fig. 4B-E). Furthermore, when $\mu \sim I_{\mathrm{b}}$, information about the signal timing stays elevated over more than two orders of magnitude of σ (blue box in Fig. 4B-E). The MI distributions for Δt_{ON} and Δt_{OFF} are similar and symmetric along the firing threshold I_{b}. Interestingly, MI from encounter duration $t_{\mathrm{dur}}^{\mathrm{enc}}$ lacks symmetry along I_{b}, as the amount of encoded information diminishes when $\mu < I_{\mathrm{b}}$ (Fig. 4D). There is a general trend of increasing MI as the input variance increases, reflecting the fact that higher frequency of threshold crossing translates to increase in coding capacity. However, MI saturates as the threshold crossing frequency saturates, which is limited by the timescales of the O-U process.

Encounter frequency and duration are critical components of the *Drosophila* odor-guided navigation strategy in turbulent plumes (8, 11, 21). Interestingly, the ORN efficiently transmits information about the duration of odor encounters $t_{\mathrm{dur}}^{\mathrm{enc}}$, but only when $\mu \geq I_{\mathrm{b}}$ (Fig. 4D), suggesting that odor encounter duration is less informative when the signal intensity is low, which is typically the case

in turbulent plumes (8, 11, 16, 18). The MI of the $t_{\mathrm{dur}}^{\mathrm{enc}}$ depends asymmetrically on $\mu - I_{\mathrm{b}}$ (Fig. 4D) because the duration of an encounter effectively disregards information encoded by fluctuations that take place when the signal is above I_{b}. When $\mu < I_{\mathrm{b}}$, any fluctuations above I_{b} result in a short encounter duration, which carries no information about the magnitude of the fluctuation. However, when $\mu > I_{\mathrm{b}}$, the signal below I_{b} rapidly drives the firing rate down to the lower bound of $0\ Hz$. This also explains why the blank duration does not exhibit asymmetry along $\mu \sim I_{\mathrm{b}}$, as blank duration only tracks signals below I_{b}. We can test this effect by modifying the O-U signal such that the O-U input above I_{b} is discretized as a single value, thereby creating an upper bound for the firing rate. Indeed, with this modified O-U signal, the MI of the $t_{\mathrm{dur}}^{\mathrm{enc}}$ becomes symmetric around I_{b} (Fig. S5).

Our results are robust to different types of input signals. We calculated the mutual information between odor timing and firing rate using as input experimentally measured time traces of odor signals experienced by walking flies freely navigating complex odor plumes (8). In these traces, the distributions of odor encounter durations and blank durations exhibit near power-law behavior over a few decades (see Fig. 1I in ref (8)) and therefore are very different from the Gaussian statistics of an O-U signal. Nonetheless, we found that the MI distributions are qualitatively similar to those obtained in response to the O-U process (compare Fig. S6B to Fig. 4). We also check that the MI becomes smaller when using temporally decorrelated Gaussian white noise as input, as expected (Fig. S5).

Mean adaptation maintains ORNs near the bifurcation point. So far, we have shown that proximity to a bifurcation enhances the transmission of olfactory information through a binary switching process. In practice, this requires that the signal mean is always positioned close to the bifurcation point I_{b}, which is an ostensibly stringent condition. How do ORNs maintain encoding fidelity in naturalistic conditions, where background stimuli intensities vary substantially between environments?

Various sensory neurons exhibit adaptation to the signal mean (40-44). A simple mechanism of mean adaptation is negative integral feedback, in which the cumulative deviation of a system's response from the baseline is fed back as an inhibitory input, pushing the system back as the response deviates from the baseline. Such negative feedback mechanisms have been observed in cellular (45, 46) and neural systems, including *Drosophila* olfaction (25, 27, 29). The adaptation in a sensory neuron is often associated with receptors and slow ion channel dynamics (47). In particular, the cytoplasmic calcium level is a critical component of adaptation in *Drosophila* ORNs (25, 29, 48, 49), suggesting the calcium influx through *Drosophila* OR is a good candidate to model the adaptive behavior.

We extend the conductance-based model (Na+K model) used above into a biophysical model of a *Drosophila* ORN (Na+K+Ca model) by incorporating the calcium influx through OR and cytoplasmic calcium-mediated regulation of the receptor activity (50) (see Methods). We model adaptation assuming that the cytoplasmic calcium dynamics are determined by the influx and the outflux of calcium ions based on the activation of the OR and the calcium pump,

$$\frac{dC}{dt} = \frac{1}{\tau_c}(g_s S - g_c C). \qquad [2]$$

Here, C is the cytoplasmic calcium concentration $[Ca^{2+}]$, S is the odor concentration, τ_c is the adaptation time scale, and g_s and g_c are constants (Fig. 5A). The ORs, together with the co-receptor Orco, form non-selective cation channels permeating sodium and calcium ions (49), and previous studies have shown that the adaptation behavior is independent of the firing activity and results from odorant binding to ORs (27, 29). We assume an active inhibition of OR by calcium ions, perhaps through a calmodulin-based mechanism (51) or calcium-dependent phosphatase-based dephosphorylation that targets Orco (48, 52) (Fig. 5B). Assuming odor binding and unbinding

is fast, we model the dependency of the input current I_s on odor concentration S and calcium concentration C as

$$I_s = \frac{g_I S}{K_s + S + \frac{C}{K_c}}, \qquad [3]$$

where g_I is a proportionality constant, K_s controls the sensitivity to the odor, and K_c determines the strength of the inhibition via calcium. Thus, the model contains a negative feedback loop modulated by calcium concentration, which relies on the fast sodium influx and the slow calcium extrusion. Combining Equations [2] and [3] with the conductance-based model (Methods), our biophysical model responds to fast changes in signal amplitude and adapts back to $\sim 30\ Hz$ following a step increase in odor concentration in accordance with experimental data (29, 53) irrespective of the background odor level (Fig. 5B).

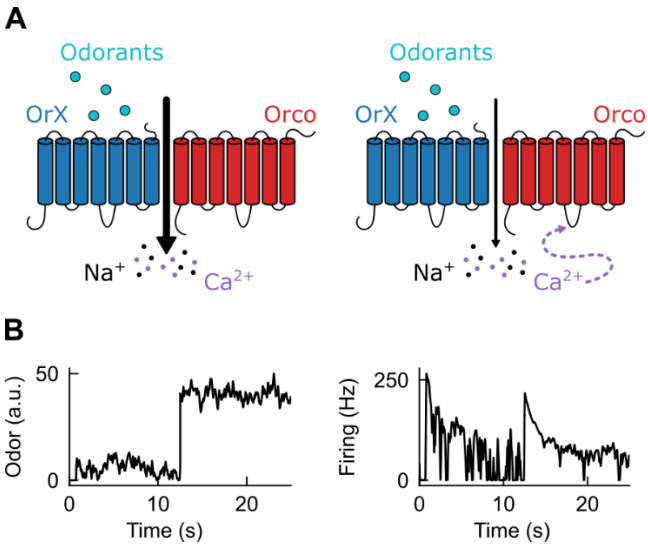

Fig. 5. Overview of the biophysical model of ORNs with calcium-mediated mean adaptation. (A) Mean adaptation in *Drosophila* ORNs is mediated by cytoplasmic calcium level. Odorant drives response by binding to olfactory receptors (OrX). Active receptors drive calcium influx along with sodium ions, which, in return, regulates the receptor activity through a calmodulin-based process or calcium-dependent phosphatase-based dephosphorylation that targets Orco, decreasing the receptor activity. Meanwhile, cytoplasmic calcium ions are sequestered in the mitochondria or pumped out, slowly recovering the sensitivity towards a fixed steady state under a continuous odor input. **(B)** The firing rate adapts to about $\sim 30\ Hz$ independent of the background odor concentration, as shown experimentally in ORN ab3A in response to ethyl acetate. To leverage bifurcation-induced benefits, we chose a steady state firing rate that corresponds to a signal slightly above the bifurcation point. Left: an odor signal trace where the mean concentration changes by an order of magnitude from 4.5 to 45 A.U. but with the same variance. Right: while the increase in odorant concentration creates a transient increase in firing rate, the ORN quickly adapts to the same average firing rate of $\sim 30\ Hz$.

The biophysical model also reproduces several key dynamical properties of ORNs. First, the firing lag, defined as the peak of the cross-correlation between the input and the response, is nearly invariant to the changes in the signal mean μ (Fig. 6A) as measured in ORNs (29). This implies that our model remains temporally precise over diverse odor concentrations. The absolute lag ($\sim 7\ ms$) suggested by the model is comparable to the smallest value of experimentally reported odor-evoked first spike latency in *Drosophila* (54). We also confirmed that the biophysical model

reproduces the gain adaptation properties of ORNs, namely the gain is inversely proportional to the mean odor intensity, thus following Weber-Fechner's law (25, 29, 53) (Fig. S7), and scales with the signal variance quantitatively similarly to the experiments (29).

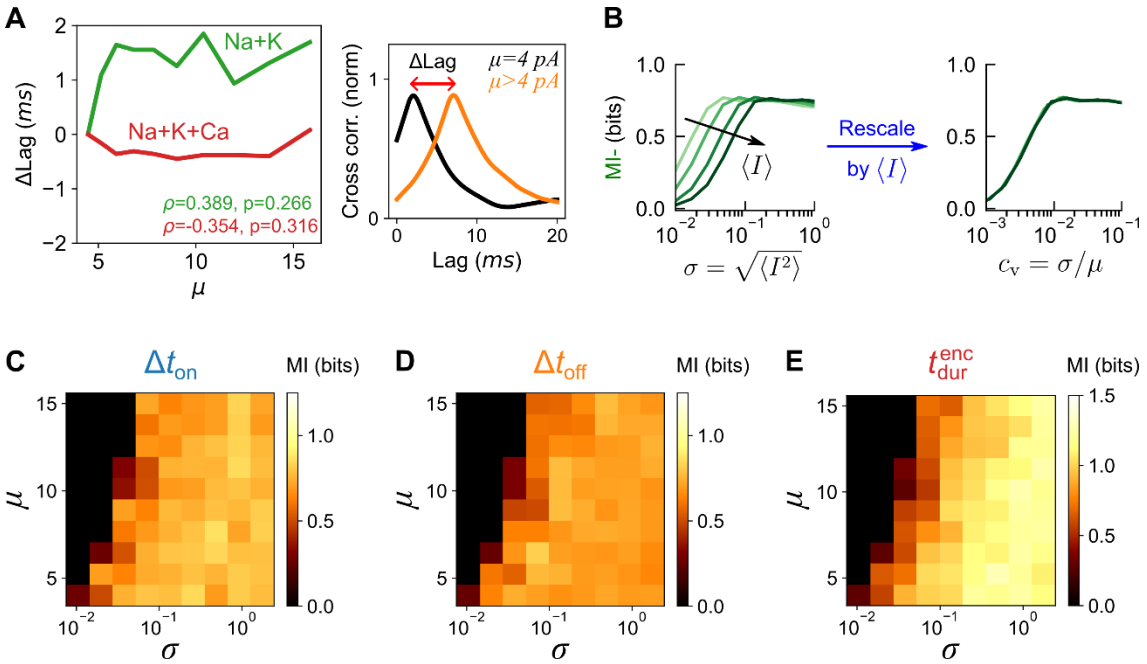

Fig. 6. Mean adaptation maintains robust bifurcation-induced information transmission across stimulus backgrounds. (A) Right: the lag between the input signal and the firing rate is quantified from the peak in the cross-correlation between the two time traces. Left: differences in firing lag ($\Delta\mathrm{lag}$) with respect to the lag at $\mu = 4\,pA$ (right, black line) as a function of the mean signal intensity μ for Na+K (green) and Na+K+Ca (red) models. The input signal standard deviation is $\sigma = 0.4$. The firing lag does not increase significantly with the mean signal intensity. ρ and p denote the Spearman correlation coefficient and the corresponding p-value. **(B)** MI- from the Na+K+Ca model using O-U odor signals with μ ranging from 4 to 15 A.U. and σ ranging from 0.01 to 3.16. Once rescaled by the signal mean, the curves collapse (right). **(C-E)** MI between the firing rate and the distributions of encounter times Δt_{ON}, blank times Δt_{OFF}, and encounter duration $t_{\mathrm{dur}}^{\mathrm{enc}}$, as a function of μ and σ given the firing rate threshold of $\sim 30\,Hz$.

To quantify the coding capacity of the biophysical model, we stimulated it with odor signals modeled as O-U processes. As before, MI- is elevated over a range of signal fluctuations. Moreover, because the gain scales inversely with the mean signal intensity, plotting MI- versus σ/μ collapses all plots onto a single curve (Fig. 6B). Therefore, the system transmits information about the fluctuations in a manner that is largely invariant with respect to the mean signal intensity. To analyze how information about odor timing is transmitted, we defined odor encounters and blanks using the baseline firing frequency of $30\,Hz$ as the crossing point instead of $I_{\mathrm{b}} = 4.54\,pA$ since mean adaptation dynamically adjusts the firing threshold. This can be viewed as a "novelty detection," where sudden deviations from the steady state are identified. We observe that adaptation to the mean signal intensity enables the model to consistently encode the timing and intensity of odor fluctuations over a wide range of mean odor concentration and variance (Fig. 6C-E).

These results demonstrate that by maintaining their operation in the vicinity of the bifurcation via a calcium-mediated adaptation mechanism, ORNs can robustly encode the intensity and timing of fluctuations in odor signal, which are critical for odor-guided navigation.

Discussion

Proximity to a bifurcation enhances information transmission in a model neuron. In this work, we quantify information transmission in a model ORN via the mutual information between the firing rate and summary statistics of the signal (odor) input. We show that information about the timing and intensity of fluctuations in odor signals are robustly encoded when the ORN firing dynamics operate close to its bifurcation. Proximity to the bifurcation also entails intrinsic variance adaptation (55, 56), further benefitting olfactory information processing. Importantly, adaptation to the signal mean can naturally drive the ORN dynamics to the bifurcation and thereby maximize information transmission without the need for an additional tuning mechanism.

Intrinsic gain control in *Drosophila* ORNs. Adaptation to variance in the input stimulus is observed in all sensory modalities (29, 57-62), and several intrinsic mechanisms for gain control have been suggested (34, 63-67).

In our biophysical model of *Drosophila* ORNs, variance adaptation occurs intrinsically as a consequence of mean or spike frequency adaptation via calcium. Interestingly, due to the large susceptibility at the bifurcation point, an adapted firing rate anywhere in the steep part of the response curve will keep the neuron very close to the firing-quiescent bifurcation. For instance, if the firing rate of *Drosophila* ORNs adapts to approximately $30\ Hz$ as we have shown previously *in vivo* (29), the corresponding injected current is within $0.5\ pA$ of the bifurcation point of our model (Fig. 1B). ORNs may therefore be able to retain a state of criticality without the need for fine-tuning. This robust tuning to a critical (bifurcation) point with enhanced signal sensitivity is reminiscent of other sensory systems, such as the thermal sensing of pit vipers (68), chemosensing in *E. coli* (69, 70), and sound amplification in the inner ear (55, 71-74). The underlying feedback motif also belongs to a wider class of integral feedback mechanisms, which exhibit precise adaptation even in networks with noisy dynamics (75).

Implication for olfactory navigation. In odor-guided navigation, temporal odor cues correlate to specific behavioral features such as moving, stopping, and turning (4, 8, 10, 11, 16, 18, 76, 77). In this work, we have shown that the frequency and duration of odor encounters are well-encoded by ORNs. We also find that their information content varies depending on context. For example, odor encounter durations are less informative when odor concentration is low as is typically the case in turbulent plumes. This is consistent with experimental findings showing that walking flies rely on odor duration to navigate diffusion-dominated plumes but less so in complex plumes, where odor encounters are brief and blanks much longer (8, 11, 18). Finally, we found that proximity to the bifurcation also enhanced information transmission when we used experimentally measured odor signals (instead of an O-U process) as input to our model. Specifically, we used time traces of odor encounters experienced by freely navigating flies in a turbulent plume (8). The statistics of these odor signals are very different from those of an O-U process. Nonetheless, we found that the MI distributions from the signal timing are similar for both the non-adapting (Na+K model; Fig. S6B) and the adapting models (Na+K+Ca model; Fig. S6C). This implies that the large information transmission at the bifurcation is broadly independent of the plume characteristics and has relevance in real-world odor-guided navigation.

Materials and Methods

Odor signal modeling. A stochastic naturalistic odor signal environment is simulated as an Ornstein-Uhlenbeck process, defined as

$$S(t+dt) = S(t) - \frac{1}{\tau_s} S(t)dt + c^{\frac{1}{2}} N(t)(dt)^{\frac{1}{2}},$$

where τ_s is the input correlation timescale, c is the diffusion constant, and $N(t)$ denotes an independent normal-distributed random variable at each time t with mean 0 and variance 1. The variance of the odor signal $S(t)$ is equal to $\sigma^2 = c\tau_s/2$.

Conductance-based neuron model. We use a 2-dimensional Hodgkin-Huxley type model known as the Morris-Lecar model (35). This model tracks potassium and sodium ion concentrations in the intra- and extracellular media as well as a leak current and exhibits a SNIC bifurcation. The potential difference across the neuronal cell membrane $V(t)$ and the fraction of potassium channel gates in the open state $n(t)$ are defined by the following sets of differential equations,

$$\frac{dV}{dt} = \left(I_s + g_L(E_L - V) + g_{Na}\, m_\infty(V)(E_{Na} - V) + n\, g_K(E_K - V)\right)/C$$

$$\frac{d}{dt} n(t) = \frac{(n_\infty - n)}{\tau_n},$$

where $m_\infty = \left(1 + e^{\frac{V_m - V}{k_m}}\right)^{-1}$ and $n_\infty = \left(1 + e^{\frac{V_n - V}{k_n}}\right)^{-1}$.

The parameters are set as $g_L = 8$, $g_{Na} = 20$, $g_K = 10$, $E_L = -80$, $E_{Na} = 60$, $E_K = -90$, $C = 1$, $V_m = -20$, $V_n = -25$, $k_m = 15$, $k_n = 5$, $\tau_n = 1$. An Ornstein-Uhlenbeck signal $S(t)$ is used as the input I_s. A timestep of $0.05\, ms$ is used to iterate the equations by the Euler method unless noted otherwise. Simulations are run for at least 20 seconds.

In principle, this model contains two voltage-gating variables, n and m, where n controls the fraction of open potassium channels, and m controls the fraction of open sodium channels. The characteristic timescale of the gating variable $m(t)$ is assumed to be much faster than fluctuations in $V(t)$ and treated as an instantaneous function of V ($m_\infty(V)$). Therefore, the current position of the system at any given time can be fully described by the values of V and n. The dynamics of other ions present in the intra- and extracellular media, such as calcium and chlorine, are not explicitly considered except when the mean adaptation is implemented.

To test the robustness of variance adaptation across different bifurcation types, we used the Hopf bifurcating model described in (78). Here, the slow current is driven by calcium, and some parameters are modified to produce a Hopf bifurcation.

$$\frac{dV}{dt} = \left(I_s + g_L(E_L - V) + g_{Ca}\, m_\infty(V)(E_{Ca} - V) + w\, g_K(E_K - V)\right)/C$$

$$\frac{dw}{dt} = \lambda_w (w_\infty - w)$$

$$\lambda_w = \phi * \cosh\left(\frac{V - V_w}{2k_w}\right)$$

$$m_\infty = \frac{1}{2}\left(1 + \tanh\left(\frac{V - V_m}{k_m}\right)\right)$$

$$w_\infty = \frac{1}{2}\left(1 + \tanh\left(\frac{V - V_w}{k_w}\right)\right)$$

The parameters are defined as: $g_L = 2$, $g_{Ca} = 4$, $g_K = 8$, $E_L = -60$, $E_{Ca} = 120$, $E_K = -84$, $C = 20$, $V_m = -1.2$, $V_w = 2$, $k_m = 18$, $k_w = 30$, $\phi = 0.04$.

Calculating the firing rate. Hodgkin-Huxley type models describe the evolution of membrane voltage with an inter-spike time on the order of milliseconds, from which we calculate the evolution of the firing rate over hundreds of milliseconds or seconds. To obtain a continuous value firing rate from the voltage-time trace generated by the model, we first run a peak-finding algorithm that binarizes all points along the time trace. The peak-finding algorithm determines a peak based on voltage spikes exceeding a membrane potential of $0\ V$. Then, a convolutional Gaussian smoothing filter with unity time-integral area is applied to the binary data to obtain a time-averaged firing rate. The standard deviation of the filter is given by $\tau_r * dt$, where τ_r is the firing rate filter timescale and dt is the simulation step size. Therefore, the filter is defined as

$$g(t) = \frac{1}{(\tau_r\, dt)\sqrt{2\pi}}\, e^{-\frac{1}{2}\left(\frac{t}{\tau_r\, dt}\right)^2}.$$

Mutual information. The mutual information between the stimulus and the firing rate is defined as the entropy of the rate minus the entropy of the rate given the corresponding value of the stimulus:

$$MI(rate, stim) = H(rate) - H(rate|stim),$$

where the entropy is defined by

$$H(rate) = -\sum P(rate)\ \log_2\big(P(rate)\big)$$

and the conditional entropy is defined by

$$H(rate|stim) = \sum P(stim = s) \sum H(rate|stim = s).$$

Numerically, mutual information can be calculated using the distributions of the stimulus and the (conditional) distributions of the firing rate. We generated a probability density function of firing rate $P(rate)$ using a histogram with 100 equal-sized bins spanning from 0 to $200\ Hz$. The entropy is computed as $H(rate) = -\sum P(rate) * \log_2 P(rate)\, dr$ where dr would be the bin size ($= 2$) when computed discretely. We confirmed that the number of data points is large enough such that the numerical MI values are robust to the error introduced by the binning process (see *SI Appendix*, Fig. S1). To calculate the conditional entropy, we also generated a probability density function for the odor signal by creating a histogram with 100 bins, with an adaptive bin size chosen such that the histogram spans $\pm 3\sigma$ of the input mean μ. When calculating mutual information about temporal odor cues, 3σ from the sample mean has been used. For each discretized stimulus bin s, we collected the distribution of firing rates observed at all corresponding times where $stim = s$, which approximates $P(rate|stim = s)$. By definition, $H(rate|stim = s) = -\sum P(rate|stim = s) * \log_2 P(rate|stim = s) * dr$ for each stimulus bin s, and the conditional entropy $H(rate|stim)$ is equal to the discrete sum of all stimulus bins times the stimulus probability.

Biophysical *Drosophila* ORN model with adaptation. As shown in the main text, we incorporate calcium-mediated adaptation by expanding upon the previously defined conductance-based neuron model (Equations [2] and [3]). The parameters in Equations [2] and [3] are as follows: $g_s = 0.76875$, $g_c = 0.0625$, $\tau_c = 250$, $g_I = 500$, $K_s = 0.1$, $K_c = 1$. A timestep of $0.1\ ms$ is used for numerical integration.

Data, Materials, and Software Availability. All original data and codes are deposited and publicly available at https://github.com/emonetlab/bifurcation-temporal-information. All other information is included in the manuscript or *SI Appendix*.

Author Contributions: K.C., W.R., I.R.G., N.K., and T.E. designed research; K.C., W.R., and N.K. performed research; K.C., W.R., N.K. and T.E. analyzed data; and K.C., W.R., I.R.G., N.K., and T.E. wrote the paper.

Acknowledgments. We thank Michael Abbott, Sam Brudner, Damon Clark, Viraaj Jayaram, and the members of the Emonet laboratory for helpful discussions and constructive comments on the manuscript. Research reported in this publication was supported by NINDS award RF1NS132840. K.C. was supported by a postdoctoral fellowship through the Swartz Foundation for Theoretical Neuroscience. I.R.G. was supported by the Deutsche Forschungsgemeinschaft Projektnummer 494077061. N.K. was supported by postdoctoral fellowships NIH F32MH118700 and NIH K99DC019397.

Competing Interest: The authors declare no competing interest.

References

1. A. Celani, E. Villermaux, M. Vergassola, Odor Landscapes in Turbulent Environments. *Physical Review X* **4** (2014).
2. G. Reddy, V. N. Murthy, M. Vergassola, Olfactory Sensing and Navigation in Turbulent Environments. *Annual Review of Condensed Matter Physics* **13**, 191-213 (2022).
3. J. A. Riffell, L. Abrell, J. G. Hildebrand, Physical processes and real-time chemical measurement of the insect olfactory environment. *J Chem Ecol* **34**, 837-853 (2008).
4. A. Mafra-Neto, R. T. Cardé, Fine-scale structure of pheromone plumes modulates upwind orientation of flying moths. *Nature* **369**, 142-144 (1994).
5. J. Murlis, J. S. Elkinton, R. T. Cardé, Odor Plumes and How Insects Use Them. *Annual Review of Entomology* **37**, 505-532 (1992).
6. C. Flügge, Geruchliche Raumorientierung von Drosophila melanogaster. *Zeitschrift für vergleichende Physiologie* **20**, 463-500 (1934).
7. J. S. Kennedy, D. Marsh, Pheromone-regulated anemotaxis in flying moths. *Science* **184**, 999-1001 (1974).
8. M. Demir, N. Kadakia, H. D. Anderson, D. A. Clark, T. Emonet, Walking Drosophila navigate complex plumes using stochastic decisions biased by the timing of odor encounters. *Elife* **9** (2020).
9. S. A. Budick, M. H. Dickinson, Free-flight responses of Drosophila melanogaster to attractive odors. *J Exp Biol* **209**, 3001-3017 (2006).
10. F. van Breugel, M. H. Dickinson, Plume-tracking behavior of flying Drosophila emerges from a set of distinct sensory-motor reflexes. *Curr Biol* **24**, 274-286 (2014).
11. E. Alvarez-Salvado *et al.*, Elementary sensory-motor transformations underlying olfactory navigation in walking fruit-flies. *Elife* **7** (2018).
12. E. Balkovsky, B. I. Shraiman, Olfactory search at high Reynolds number. *Proc Natl Acad Sci U S A* **99**, 12589-12593 (2002).
13. A. M. M. Matheson *et al.*, A neural circuit for wind-guided olfactory navigation. *Nat Commun* **13**, 4613 (2022).
14. P. Szyszka, T. Emonet, T. L. Edwards, Extracting spatial information from temporal odor patterns: insights from insects. *Curr Opin Insect Sci* **59**, 101082 (2023).
15. A. Sehdev, Y. G. Mohammed, T. Triphan, P. Szyszka, Olfactory Object Recognition Based on Fine-Scale Stimulus Timing in Drosophila. *iScience* **13**, 113-124 (2019).
16. V. Jayaram, N. Kadakia, T. Emonet, Sensing complementary temporal features of odor signals enhances navigation of diverse turbulent plumes. *Elife* **11** (2022).
17. G. Raiser, C. G. Galizia, P. Szyszka, Ephaptic coupling between olfactory receptor neurons is sensitive to relative stimulus timing: Implications for odour source discrimination. *bioRxiv* 10.1101/2023.11.27.568881 (2023).

18. V. Jayaram, A. Sehdev, N. Kadakia, E. A. Brown, T. Emonet, Temporal novelty detection and multiple timescale integration drive Drosophila orientation dynamics in temporally diverse olfactory environments. *PLoS Comput Biol* **19**, e1010606 (2023).
19. S. D. Boie *et al.*, Information-theoretic analysis of realistic odor plumes: What cues are useful for determining location? *PLoS Comput Biol* **14**, e1006275 (2018).
20. I. J. Park *et al.*, Neurally Encoding Time for Olfactory Navigation. *PLoS Comput Biol* **12**, e1004682 (2016).
21. N. Kadakia *et al.*, Odour motion sensing enhances navigation of complex plumes. *Nature* **611**, 754-761 (2022).
22. J. Murlis, M. A. Willis, R. T. Cardé, Spatial and temporal structures of pheromone plumes in fields and forests. *Physiological Entomology* **25**, 211-222 (2001).
23. G. Si *et al.*, Structured Odorant Response Patterns across a Complete Olfactory Receptor Neuron Population. *Neuron* **101**, 950-962 e957 (2019).
24. C. Martelli, J. R. Carlson, T. Emonet, Intensity invariant dynamics and odor-specific latencies in olfactory receptor neuron response. *J Neurosci* **33**, 6285-6297 (2013).
25. L. H. Cao *et al.*, Distinct signaling of Drosophila chemoreceptors in olfactory sensory neurons. *Proc Natl Acad Sci U S A* **113**, E902-911 (2016).
26. J. Cafaro, Multiple sites of adaptation lead to contrast encoding in the Drosophila olfactory system. *Physiol Rep* **4** (2016).
27. K. I. Nagel, R. I. Wilson, Biophysical mechanisms underlying olfactory receptor neuron dynamics. *Nat Neurosci* **14**, 208-216 (2011).
28. K. I. Nagel, E. J. Hong, R. I. Wilson, Synaptic and circuit mechanisms promoting broadband transmission of olfactory stimulus dynamics. *Nat Neurosci* **18**, 56-65 (2015).
29. S. Gorur-Shandilya, M. Demir, J. Long, D. A. Clark, T. Emonet, Olfactory receptor neurons use gain control and complementary kinetics to encode intermittent odorant stimuli. *Elife* **6** (2017).
30. P. Szyszka, R. C. Gerkin, C. G. Galizia, B. H. Smith, High-speed odor transduction and pulse tracking by insect olfactory receptor neurons. *Proc Natl Acad Sci U S A* **111**, 16925-16930 (2014).
31. K. S. Gaudry, P. Reinagel, Benefits of contrast normalization demonstrated in neurons and model cells. *J Neurosci* **27**, 8071-8079 (2007).
32. Y. Yu, T. S. Lee, Dynamical mechanisms underlying contrast gain control in single neurons. *Phys Rev E Stat Nonlin Soft Matter Phys* **68**, 011901 (2003).
33. C. A. Matulis, J. Chen, A. D. Gonzalez-Suarez, R. Behnia, D. A. Clark, Heterogeneous Temporal Contrast Adaptation in Drosophila Direction-Selective Circuits. *Curr Biol* **30**, 222-236 e226 (2020).
34. I. Nemenman, Gain control in molecular information processing: lessons from neuroscience. *Phys Biol* **9**, 026003 (2012).
35. C. Morris, H. Lecar, Voltage oscillations in the barnacle giant muscle fiber. *Biophys J* **35**, 193-213 (1981).
36. K. S. Gaudry, P. Reinagel, Contrast adaptation in a nonadapting LGN model. *J Neurophysiol* **98**, 1287-1296 (2007).
37. A. L. Fairhall, G. D. Lewen, W. Bialek, R. R. de Ruyter Van Steveninck, Efficiency and ambiguity in an adaptive neural code. *Nature* **412**, 787-792 (2001).
38. C. D. Wilson, G. O. Serrano, A. A. Koulakov, D. Rinberg, A primacy code for odor identity. *Nat Commun* **8**, 1477 (2017).
39. R. Shusterman, M. C. Smear, A. A. Koulakov, D. Rinberg, Precise olfactory responses tile the sniff cycle. *Nat Neurosci* **14**, 1039-1044 (2011).
40. J. Clemens, N. Ozeri-Engelhard, M. Murthy, Fast intensity adaptation enhances the encoding of sound in Drosophila. *Nat Commun* **9**, 134 (2018).
41. J. Benda, Neural adaptation. *Curr Biol* **31**, R110-R116 (2021).
42. K. I. Nagel, A. J. Doupe, Temporal processing and adaptation in the songbird auditory forebrain. *Neuron* **51**, 845-859 (2006).
43. D. H. Foster, Color constancy. *Vision Res* **51**, 674-700 (2011).

44. T. Kurahashi, A. Menini, Mechanism of odorant adaptation in the olfactory receptor cell. *Nature* **385**, 725-729 (1997).
45. S. M. Block, J. E. Segall, H. C. Berg, Impulse responses in bacterial chemotaxis. *Cell* **31**, 215-226 (1982).
46. T. M. Yi, Y. Huang, M. I. Simon, J. Doyle, Robust perfect adaptation in bacterial chemotaxis through integral feedback control. *Proc Natl Acad Sci U S A* **97**, 4649-4653 (2000).
47. A. I. Weber, K. Krishnamurthy, A. L. Fairhall, Coding Principles in Adaptation. *Annu Rev Vis Sci* **5**, 427-449 (2019).
48. H. Guo, D. P. Smith, Odorant Receptor Desensitization in Insects. *J Exp Neurosci* **11**, 1179069517748600 (2017).
49. D. Wicher, F. Miazzi, Functional properties of insect olfactory receptors: ionotropic receptors and odorant receptors. *Cell Tissue Res* **383**, 7-19 (2021).
50. J. Benda, A. V. Herz, A universal model for spike-frequency adaptation. *Neural Comput* **15**, 2523-2564 (2003).
51. L. Mukunda, F. Miazzi, S. Kaltofen, B. S. Hansson, D. Wicher, Calmodulin modulates insect odorant receptor function. *Cell Calcium* **55**, 191-199 (2014).
52. V. Sargsyan *et al.*, Phosphorylation via PKC Regulates the Function of the Drosophila Odorant Co-Receptor. *Front Cell Neurosci* **5**, 5 (2011).
53. N. Kadakia, T. Emonet, Front-end Weber-Fechner gain control enhances the fidelity of combinatorial odor coding. *Elife* **8** (2019).
54. A. Egea-Weiss, A. Renner, C. J. Kleineidam, P. Szyszka, High Precision of Spike Timing across Olfactory Receptor Neurons Allows Rapid Odor Coding in Drosophila. *iScience* **4**, 76-83 (2018).
55. A. J. Hudspeth, F. Julicher, P. Martin, A critique of the critical cochlea: Hopf--a bifurcation--is better than none. *J Neurophysiol* **104**, 1219-1229 (2010).
56. A. Erez, T. A. Byrd, M. Vennettilli, A. Mugler, Cell-to-Cell Information at a Feedback-Induced Bifurcation Point. *Phys Rev Lett* **125**, 048103 (2020).
57. D. G. Albrecht, D. B. Hamilton, Striate cortex of monkey and cat: contrast response function. *J Neurophysiol* **48**, 217-237 (1982).
58. B. Wark, B. N. Lundstrom, A. Fairhall, Sensory adaptation. *Curr Opin Neurobiol* **17**, 423-429 (2007).
59. N. Brenner, W. Bialek, R. de Ruyter van Steveninck, Adaptive rescaling maximizes information transmission. *Neuron* **26**, 695-702 (2000).
60. J. L. Gardner *et al.*, Contrast adaptation and representation in human early visual cortex. *Neuron* **47**, 607-620 (2005).
61. D. Chander, E. J. Chichilnisky, Adaptation to temporal contrast in primate and salamander retina. *J Neurosci* **21**, 9904-9916 (2001).
62. F. Rieke, Temporal contrast adaptation in salamander bipolar cells. *J Neurosci* **21**, 9445-9454 (2001).
63. S. Hong, B. N. Lundstrom, A. L. Fairhall, Intrinsic gain modulation and adaptive neural coding. *PLoS Comput Biol* **4**, e1000119 (2008).
64. K. W. Latimer *et al.*, Multiple Timescales Account for Adaptive Responses across Sensory Cortices. *J Neurosci* **39**, 10019-10033 (2019).
65. R. A. Mease, M. Famulare, J. Gjorgjieva, W. J. Moody, A. L. Fairhall, Emergence of adaptive computation by single neurons in the developing cortex. *J Neurosci* **33**, 12154-12170 (2013).
66. M. Diaz-Quesada, M. Maravall, Intrinsic mechanisms for adaptive gain rescaling in barrel cortex. *J Neurosci* **28**, 696-710 (2008).
67. A. Borst, V. L. Flanagin, H. Sompolinsky, Adaptation without parameter change: Dynamic gain control in motion detection. *Proc Natl Acad Sci U S A* **102**, 6172-6176 (2005).
68. I. R. Graf, B. B. Machta, A bifurcation integrates information from many noisy ion channels and allows for milli-Kelvin thermal sensitivity in the snake pit organ. *Proc Natl Acad Sci U S A* **121**, e2308215121 (2024).

69. J. M. Keegstra, F. Avgidis, Y. Mulla, J. S. Parkinson, T. S. Shimizu, Near-critical tuning of cooperativity revealed by spontaneous switching in a protein signalling array. *arXiv* 10.1101/2022.12.04.518992 (2023).
70. D. M. Sherry, S. J. Bryant, I. R. Graf, T. Emonet, B. B. Machta, Lattice ultrasensitivity produces large gain in E. coli chemosensing. *arXiv* (2024).
71. A. J. Hudspeth, Integrating the active process of hair cells with cochlear function. *Nat Rev Neurosci* **15**, 600-614 (2014).
72. S. Camalet, T. Duke, F. Julicher, J. Prost, Auditory sensitivity provided by self-tuned critical oscillations of hair cells. *Proc Natl Acad Sci U S A* **97**, 3183-3188 (2000).
73. Y. Choe, M. O. Magnasco, A. J. Hudspeth, A model for amplification of hair-bundle motion by cyclical binding of Ca2+ to mechanoelectrical-transduction channels. *Proc Natl Acad Sci U S A* **95**, 15321-15326 (1998).
74. V. M. Eguiluz, M. Ospeck, Y. Choe, A. J. Hudspeth, M. O. Magnasco, Essential nonlinearities in hearing. *Phys Rev Lett* **84**, 5232-5235 (2000).
75. C. Briat, A. Gupta, M. Khammash, Antithetic Integral Feedback Ensures Robust Perfect Adaptation in Noisy Biomolecular Networks. *Cell Syst* **2**, 15-26 (2016).
76. R. T. Carde, M. A. Willis, Navigational strategies used by insects to find distant, wind-borne sources of odor. *J Chem Ecol* **34**, 854-866 (2008).
77. S. D. Stupski, F. van Breugel, Wind Gates Search States in Free Flight. *bioRxiv* 10.1101/2023.11.30.569086 (2024).
78. B. Ermentrout, *Simulating, analyzing, and animating dynamical systems : a guide to XPPAUT for researchers and students*, Software, environments, tools (Society for Industrial and Applied Mathematics, Philadelphia, 2002), pp. xiv, 290 p.

Supporting Information

MI is not sensitive to binning in the context of our analysis. Numerical calculation of MI is prone to the binning process. Either too small or too large bin sizes can introduce errors to the estimated MI, especially when the number of data points is finite and contains missing values (e.g., not all values in one variable have a corresponding pair in another variable). Fortunately, we can generate signals for an arbitrarily long time and simulate the respective firing rate perfectly. We find that our system operates in a regime where the histograms of the variables are smooth, such that the histogram-based numerical MI calculation is robust enough.

According to Steuer *et al.* (1), the systematic error introduced in MI by the binning process can be estimated by

$$err = \frac{m_{xy} - m_x - m_y + 1}{2N}.$$

Here, m denotes the number of discrete states for two variables (x and y), while N denotes the number of data points. In our study, with $m_{stim} = m_{rate} = 100$, $m_{stim,rate} = 10^4$, and $N \geq 10^6$, our estimated error in MI is around 0.0049, which is significantly smaller than the scale of MI.

Additionally, we scanned through combinations of bin numbers m_{stim} and m_{rate} to ensure that our system is operating in a smooth regime. We find that for all combinations of bin numbers, MI stays consistent: MI goes over 1 bit and responds similarly to the increase in signal variance (Fig. S1). The combinations of bin numbers tested include those suggested by various well-established systematic criteria (2).

The revised linear-nonlinear model exhibits elevated coding capacity and variance adaptation. Linear-nonlinear models are widely used to describe the phenomenological properties of neural dynamics and were previously used to emulate signal variance adaptation (3). A traditional LN model includes two parts: a convolution with a smoothing filter (e.g., Gaussian), followed by a nonlinear compression (e.g., a rectified linear unit, ReLU), which simulates the effect of saturation (Fig. S4A, red). Under this framework, the model does not exhibit variance adaptation (Fig. S4B, red). However, when we substitute the rectified linear unit for the SNIC bifurcating I-r curve (Fig. 1B), the imperfect gain control is recovered (Fig. S4B, orange). Once the input I crosses the spiking threshold, dr/dI decreases as I increases, pushing the system farther away from the bifurcation point, such that greater fluctuations in I are required to drive the same change in firing rate.

In Hodgkin-Huxley type neurons, the time to spike reflects the weighted average of stimulus intensity over the relatively small inter-spike intervals. However, to construct a continuous firing rate from discrete firing events, the spiking events must be smoothed by a filter whose width is significantly greater than the inter-spike period. In terms of LN models, this means applying linear filtering *after* the nonlinear compression to make our analyses analogous to that of the Hodgkin-Huxley type model. This new architecture, which we call the nonlinear-linear (NL) model (Fig. S4A, green and blue), retains variance adaptation (Fig. S4B, green and blue) and demonstrates a significant improvement (~15%) in coding capacity with respect to their LN model counterparts (Fig. S4C). Replacing the architecture from LN to NL smoothens the transition from activity to quiescence, allowing information about the time since the excursion into the quiescent regime to be extracted. With a correlated input like an O-U signal, the system can encode information about the stimulus even when the neuron is close to the quiescent regime, providing distinct advantages over traditional LN models.

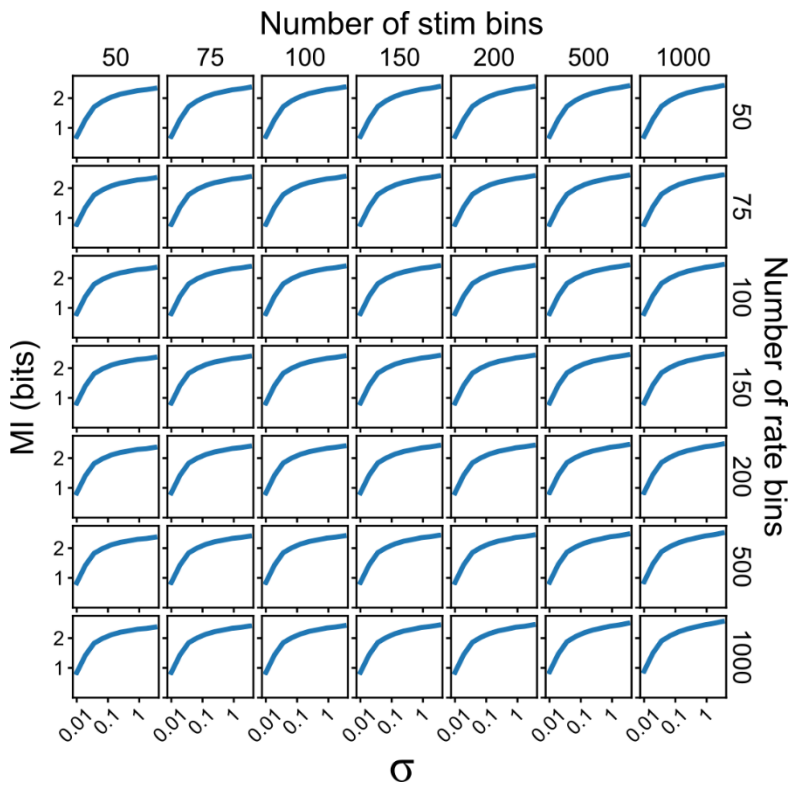

Fig. S1. MI encodes more than 1 bit of information regardless of the bin size. Discretized MI calculation can be influenced by the number of bins, but for our system, MI seems to stay relatively consistent. $I_{\mathrm{b}} = 4.54\ pA$ is used.

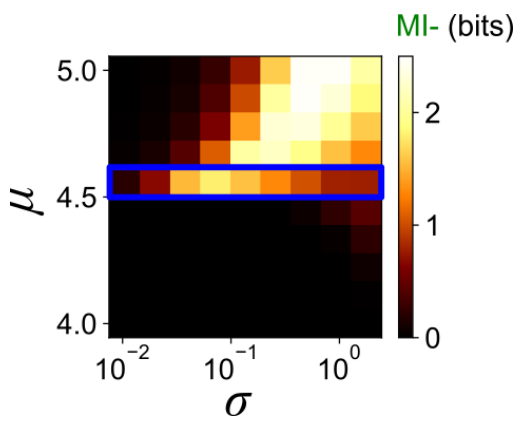

Fig. S2. The variance adaptation is due to the proximity to a bifurcation and not the signal process. MI- as a function of the mean μ and standard deviation σ using a Gaussian white noise as the input current. The blue box corresponds to $\mu \sim I_{\mathrm{b}} = 4.54\ pA$. When μ is close to $I_{\mathrm{b}} = 4.54\ pA$, MI- stays elevated over the wide range of σ.

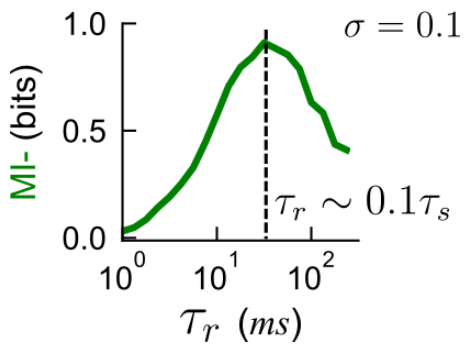

Fig. S3. MI- is maximized around $\tau_r \sim 1/10\ \tau_s$. A vertical cross-section of Fig. 3C at $\sigma \sim 0.1$. This relationship is consistent across different σ.

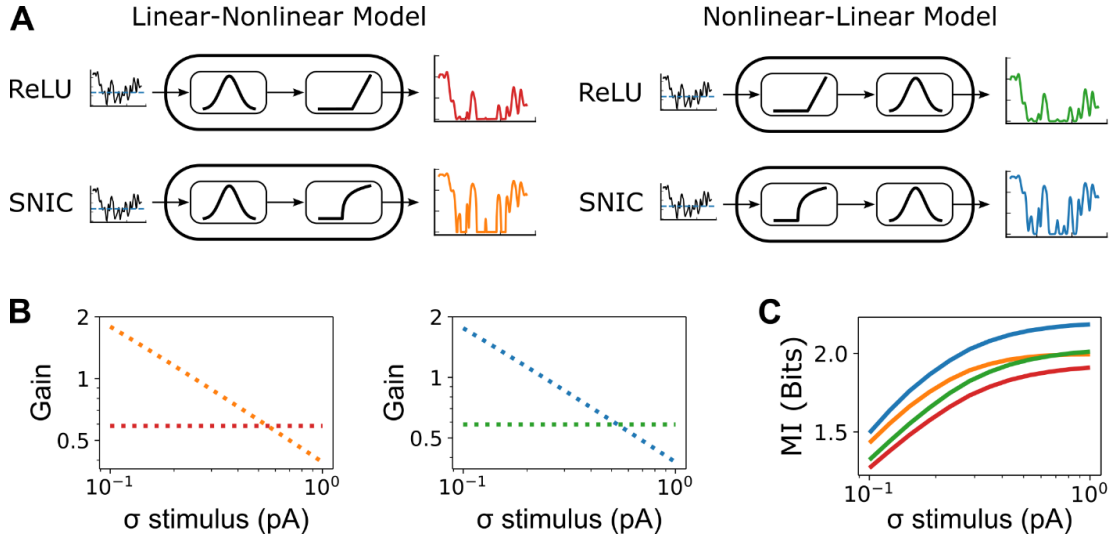

Fig. S4. Using a SNIC bifurcation in a nonlinear-linear architecture model allows variance adaptation and high information throughput. (A) Four different models can be generated using a combination of ReLU or SNIC nonlinearities in LN or NL architecture. Red: LN-ReLU, orange: LN-SNIC, green: NL-ReLU, blue: NL-SNIC. **(B)** Gain, defined as the ratio of the standard deviation of the model response to the standard deviation of the stimulus, plotted for LN models and NL models for an O-U stimulus with σ ranging from 0.1 to 1 pA. Although the order of operations of the model architecture does not affect the gain, gain control is only observed in models that use the SNIC filter (orange and blue). **(C)** The mutual information between the stimulus and the response for the four models. The same color code is used. NL model with the SNIC filter encodes the highest amount of information.

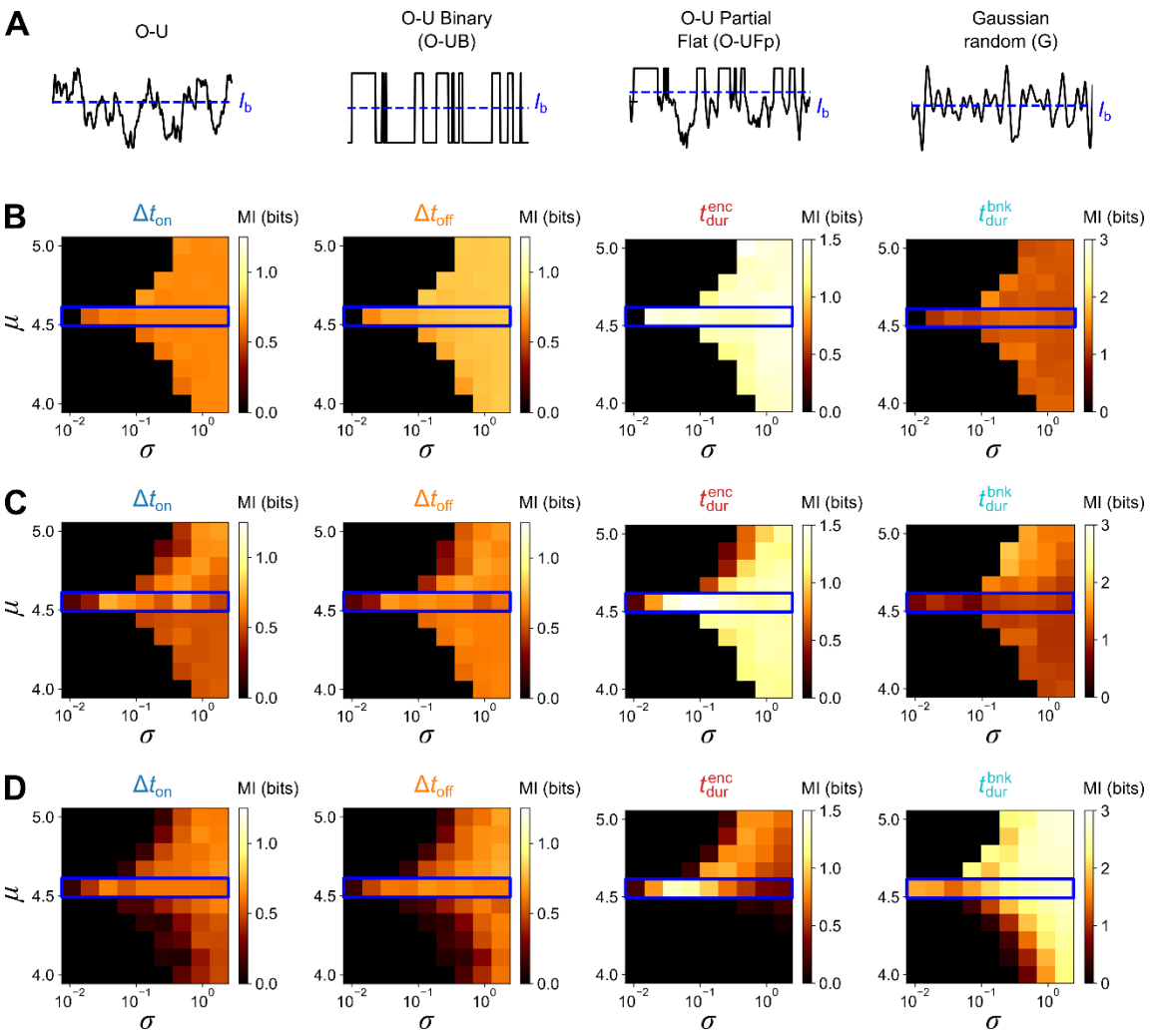

Fig. S5. The coding capacity for the signal timing is affected by fluctuations and is independent of the signal process. (A) A schematic illustrating traces of different signal types, including the Ornstein–Uhlenbeck process (O-U), a binarized Ornstein–Uhlenbeck process (O-UB), a partially flattened Ornstein–Uhlenbeck process (O-UFp), and a Gaussian random (G). **(B)** MI between the distributions of encounter times Δt_{ON} (first column), blank times Δt_{OFF} (second column), encounter duration $t_{\mathrm{dur}}^{\mathrm{enc}}$ (third column), and blank duration $t_{\mathrm{dur}}^{\mathrm{bnk}}$ (fourth column) and the firing rate r as a function of signal mean μ and standard deviation σ using a fully-binarized O-UB input. **(C)** Same as (B) for a partially reduced O-UFp as the input signal, where only the fluctuations above I_{b} are removed. **(D)** Same as (B) for Gaussian white noise as the input signal.

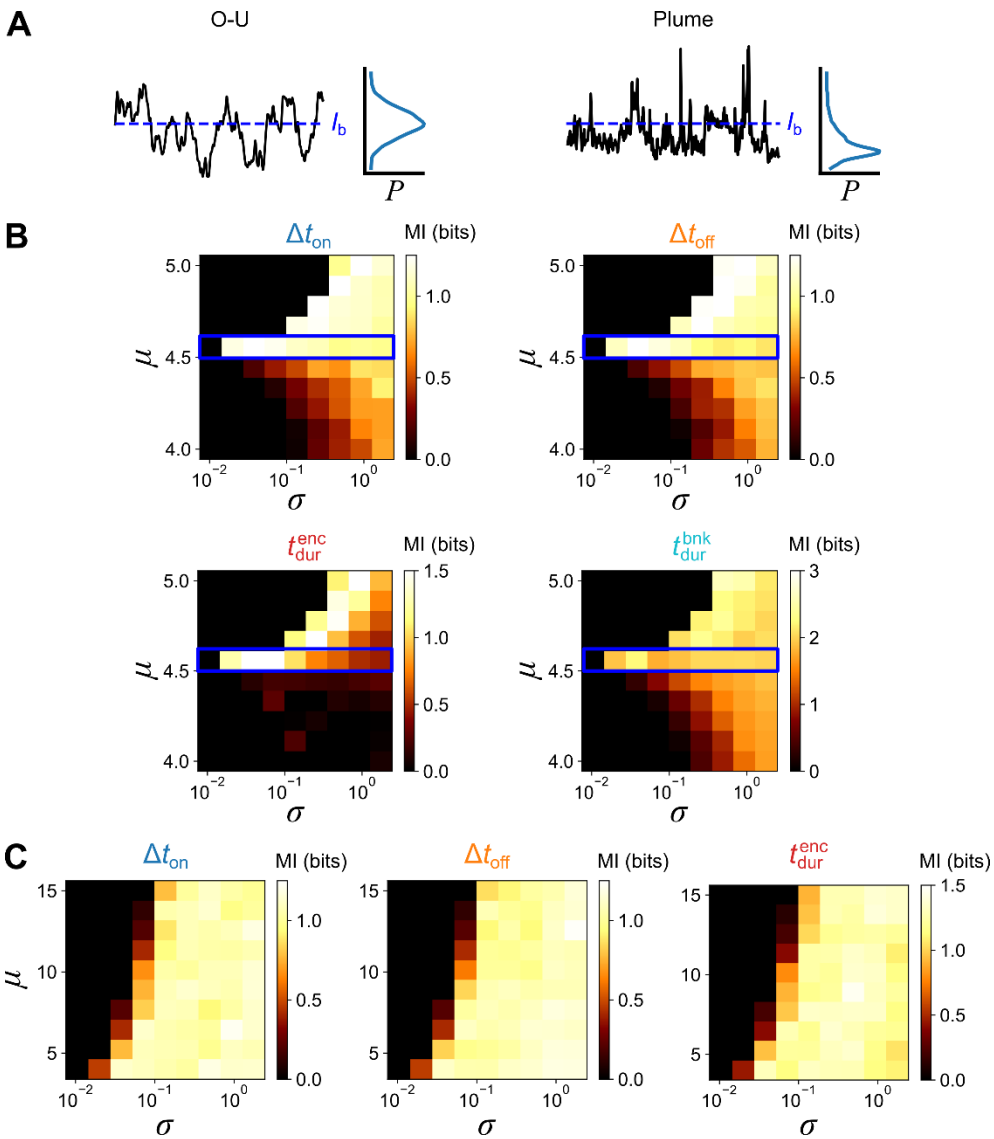

Fig. S6. The coding capacity for the signal timing using experimentally measured odor traces encountered by freely navigating flies. (A) The odor signal fruit flies experience in turbulent plumes differs from the O-U signal. The time trace of real plume concentrations encountered by an animal shows a long-tailed distribution, and the distributions of odor encounter and blank durations exhibit near power-law behavior. **(B)** MI between the distributions of encounter times Δt_{ON}, blank times Δt_{OFF}, encounter duration $t_{\mathrm{dur}}^{\mathrm{enc}}$, and blank duration $t_{\mathrm{dur}}^{\mathrm{bnk}}$ and the firing rate r as a function of signal mean μ and standard deviation σ using a real plume signal in the non-adapting Na+K model. The real plume time traces are shifted and rescaled to fit the denoted μ and σ. **(C)** Same as (B) but using the adapting Na+K+Ca model with the firing rate threshold of $\sim 30\ Hz$.

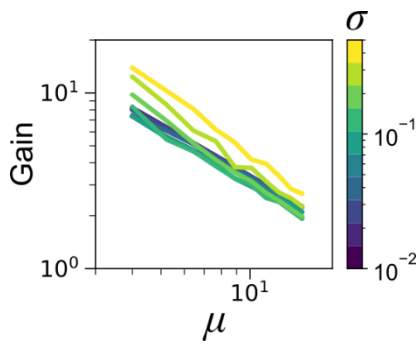

Fig. S7. The biophysical model exhibits gain scaling consistent with the Weber-Fechner law. The color bar corresponds to the σ from 0.01 to 0.5.